Fatigue Crack Growth Mechanisms in High-Pressure Die-Cast Magnesium Alloys

HAITHAM EL KADIRI, M.F. HORSTEMEYER, J.B. JORDON, and YIBIN XUE

Microstructure-affected micromechanisms of fatigue crack growth operating near the limit plasticity regime were experimentally identified for the four main commercial high-pressure die-cast (HPDC) magnesium alloys: AM50, AM60, AZ91, and AE44. These fatigue micromechanisms manifested by the concomitant effects of casting pores, interdendritic Al-rich solid solution layer, β-phase particles, Mn-rich inclusions, rare earth-rich intermetallics, dendrite cell size, and surface segregation phenomena. These concomitant mechanisms clearly delineated the fatigue durability observed for the AM50, AM60, AZ91, and AE44 Mg alloys in both the low- and high-cycle fatigue regimes.

DOI: 10.1007/s11661-007-9328-x

I. INTRODUCTION

WEIGHT reduction is considered a primary design metric for increasing fuel efficiency and reducing automotive and aircraft component costs.[1] High-strength and lightweight aluminum alloys, exemplified by the 6000-series grades, have been used successfully as structural automotive components. However, additional significant weight and process cost reductions could be achieved if magnesium alloys become the foremost replacement for heavier materials.[2]

Contemporary Mg alloys possess the highest strength-to-weight ratio among all structural metals, with a density of 1.74 Mg/m^3. One ongoing major barrier to the industrialization of Mg alloys in automotive applications is their relatively low resistance to fatigue and corrosion service conditions.[3–6] These low fatigue and corrosion resistances of Mg alloys are mainly due to the material's physical properties. The Mg alloys are remarkably reactive and exceptionally susceptible to forming microstructural singularities during shaping processes.[3] To overcome the detrimental effects of these microstructural singularities, current material selection, manufacturing, and design optimization methods resort to overdesigning. The resulting increased safety factors counteract the original attractive attributes of Mg alloys that have a high stiffness-to-weight ratio.

To fully achieve the broad benefit of these magnesium alloys, the mechanisms of fatigue and corrosion must be rigorously linked to microstructural properties. Corrosion resistance has been the primary concern in the recent research work topics.[4–6] However, too little effort has been deployed in identifying microstructural explanations for fatigue crack growth mechanisms. Moreover, the results reported by various authors have sometimes been controversial and only treated Mg-based alloys separately.[7–17] A study of the fatigue crack growth mechanisms of the AM50 Mg alloy was recently reported by the present authors.[17]

In this article, we quantify the microstructural defects to fatigue crack incubation, microstructurally small cracks (MSC), physically small cracks (PSC), and long cracks (LC) for four commercially dominant high-pressure die-cast (HPDC) magnesium alloys: AM50, AM60, AZ91, and AE44. A full description of the incubation, MSC, PSC, and LC regimes was reported in Reference 18. We performed scanning electron microscope (SEM) fractographic analyses on specimens tested in a fully-reversed strain control condition at a single strain amplitude. The microstructural defects relevant to fatigue crack growth are identified and analyzed using backscatter electron mode and electron probe microanalyses (EPMA).

II. EXPERIMENTAL

For each alloy, plates with dimensions of $100 \times 150 \times 3$ mm were cast in a permanent mold by a high-pressure die-casting technique. Flat dog-bone-shaped samples having a 25.4-mm gage length, a 10-mm gage width, and a 3-mm thickness were extracted from the center of the plate for fatigue testing. This implies that the two large faces of the rectangular specimens exhibited the original skin microstructure at the free surface. Only the sections through the thickness (the 3-mm-thick edges) were subjected to the milling process. Actually, we believe that the machining had a minor effect on crack incubation, because in all specimens, the cracks started at shrinkage or cast pores emerging at the free surface. The skin surface was not subjected to any post-surface treatment. As such, we did not perform X-ray diffraction (XRD) analyses. The skin microstructure generated by the high die pressure had a

HAITHAM EL KADIRI, Assistant Research Professor, M.F. HORSTEMEYER, Chair Professor in Computational Solid Mechanics, J.B. JORDON, Postdoctoral Candidate, and YIBIN XUE, Assistant Research Professor, are with the Center for Advanced Vehicular Systems, Mississippi State University, Starkville, MS 39762-9627, USA. Contact e-mail: elkadiri@cavs.msstate.edu
Manuscript submitted February 3, 2007.
Article published online December 4, 2007

noticeable effect on the mechanical properties of the material.[19]

Constant amplitude fatigue tests were performed with an MTS servohydraulic machine (MTS Systems Corporation, Eden Prairie, MN) in strain control under a condition of $R = -1$ (fully reversed), at a frequency of 0.5 Hz, and at multiple strain amplitudes. The tests were conducted at room temperature in laboratory air. Fractographic analyses were performed using a JEOL* field-emission gun (FEG)-SEM.

*JEOL is a trademark of Japan Electron Optics Ltd., Tokyo.

For the AZ91 alloy, we also performed fatigue tests on round samples, but only at a strain amplitude of 0.3 pct. These samples were cast directly into a round shape, and no post machining or sample preparation was performed after casting.

The microstructure was examined by means of an FEG-SEM on polished samples using either secondary electron imaging (SEI) or backscatter electron imaging (BSEI). The specimens were polished to a mirror-surface finish using standard metallographic equipment. Water contact was avoided, to prevent the formation of surface hydroxides; thus, grinding and polishing were conducted using a mixture of 1 part glycerine and 3 parts ethanol. The grain size of each alloy was measured by the conventional linear intercept method, using optical microscopy (OM). In this approach, a test pattern of lines of known length was randomly laid over a plane section, and the individual intercept lengths across several grain boundaries were measured. An average grain size was calculated by dividing the length of a segment by the total number of intersections occurring within the grain boundaries.

The EPMA were also performed to reveal the nature of the phases in the matrix detected at high magnification with the BSEI technique. The quantitative EPMA chemical composition results of all four alloys are reported in Table I, in comparison with those provided by the industrial supplier General Motors Worldwide (GMW). The element contents were averaged over ten analyzed windows with a surface area of 50×50 μm.

III. MICROSTRUCTURE OF ALLOYS

In order for the fractographic analyses to be relevant, we characterized the microstructure of the four alloys. The FEG-SEM micrographs and X-ray mapping analyses using EPMA are shown in Figures 1 through 8. Several observations can be made from these figures.

For the AM50, AM60, and AZ91 alloys, Al enrichment took place to different extents in the α-Mg dendrite cells (Figures 1 through 6). These Al enrichment gradients comprised a bulky Al-poor dendrite core, followed by a eutectic Al-rich solid solution band at the dendrite cell boundary. Within this Al-rich eutectic band, β-$Mg_{17}Al_{12}$ phase precipitated in lamellar morphology. This phase was shown to have a cubic crystal structure.[20] The presence of the β compound increased as the Al content increased in the alloys. Thicker strips of both β-phase and Al-rich eutectic solid solution bands were observed in the AM60 alloy than in the AM50 alloy (Figures 1 through 3). For the AZ91 alloy, the Al-rich eutectic took a completely divorced form, with massive and continuous precipitation of the β phase.[21]

For the AM50, AM60, and AZ91 alloys, round particles rich in Al and Mn were observed in the Al-rich eutectic phase. These particles were correlated with the presence of β-phase particles and reached over 10 μm in size. The Mn-rich inclusions were demonstrated to present in the form of a Mn-poor round phase overlaid by smaller hexagonal Al_8Mn_5 particles.[17] The hexagonal Al_8Mn_5 particles were revealed to have a hexagonal crystallographic structure.[20]

For the AE44 alloy (Figures 7 and 8), extensive concurrent enrichment of Al and mischmetal (RE) occurred as fine platelets decorating the interdendritic eutectic. This enrichment may correspond to the $Al_{11}RE_3$ phase reported in Reference 20. In marked contrast to the other alloys, the β-$Mg_{17}Al_{12}$ and Al_8Mn_5 were very scarce in the AE44. These noticeably lower contents of the β-$Mg_{17}Al_{12}$ and Al_8Mn_5 compounds can be explained by the higher affinity of Al to the RE elements that have significantly lower solubility in Mg, compared to those of Al and Mn.

For the AM50 and AM60 alloys, the dendrite cells were relatively small and had an average linear intercept size of 9 μm. However, large presolidified

Table I. Quantitative Chemical Compositions (in Weight) for All Four Alloys Obtained by Means of EPMA in Comparison with Those Provided by General Motors (Material Supplier)

AM50	Mg	Al	Mn	Zn	Si	Fe	Fe/Mn	O
GMW	bal	4.4 to 5.5	0.26 to 0.6	0.2 max	0.1 max	0.005 max	0.015 max	NI
EPMA	93.66	4.80	0.31	0.027	0.15	0.012	0.08	2.8
AZ91	Mg	Al	Mn	Zn	Si	Fe	Fe/Mn	O
GMW	bal	8.3 to 9.7	0.15 to 0.5	0.35 to 1	0.1 max	0.005 max	0.032 max	NI
EPMA	93.17	8.13	0.20	0.82	0.18	0.0038	0.019	2.75
AM60	Mg	Al	Mn	Zn	Si	Fe	Fe/Mn	O
GMW	bal	5.5 to 6.5	0.24 to 0.6	0.2 max	0.1 max	0.005 max	0.021 max	NI
EPMA	93.17	5.3	0.237	0.016	0.20	0.0128	0.054	2.9
AE44	Mg	Al	Mn	Zn	Si	Fe	Ce + La	O
GMW	bal	3.5 to 4.5	0.15 to 0.5	0.2 max	0.1 max	0.005 max	3.5 to 4.5	NI
EPMA	87.88	3.44	0.18	0.015	0.005	0.0038	1.9	0.88

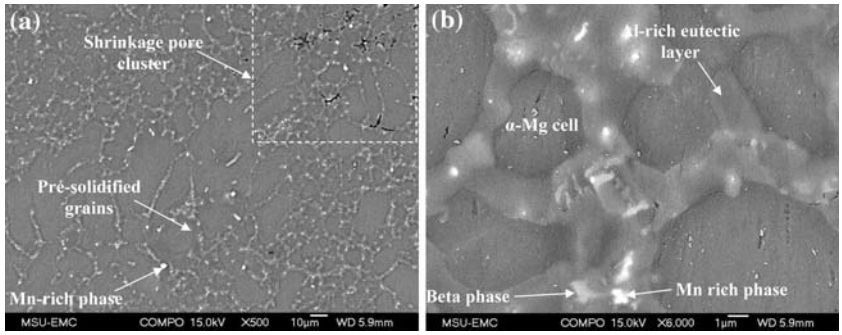

Fig. 1—Backscatter FEG-SEM micrographs of a polished AM50 sample cut from the grip section of a fractured fatigue specimen showing (*a*) an overall view of the microstructure depicting shrinkage pore clusters and an Al-rich eutectic layer fully occupying the dendrite cell boundaries and large presolidified grains and (*b*) a higher-magnification image revealing the formation of the beta phase and Mn-rich intermetallics within the Al-rich eutectic layer.

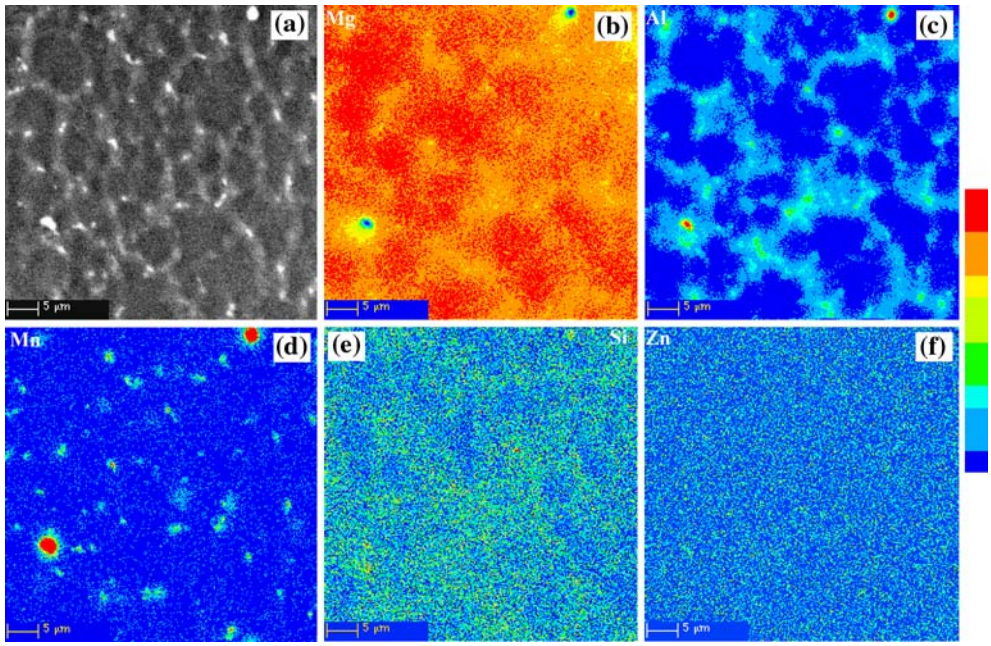

Fig. 2—EPMA X-ray maps of a mirror-finish AM50 sample surface, shown in (*a*) backscattered mode, revealing (*b*) a Mg-concentration contour, (*c*) an Al-concentration contour delineating the Al-rich eutectic layer, beta phase, and Mn-rich inclusions, (*d*) a Mn-concentration contour showing the size and distribution of the Mn-rich inclusions, (*e*) a Si-concentration contour revealing the association of this element with the Al-rich eutectic region, and (*f*) a Zn-concentration contour showing no localization of this element in the AM50 alloy.

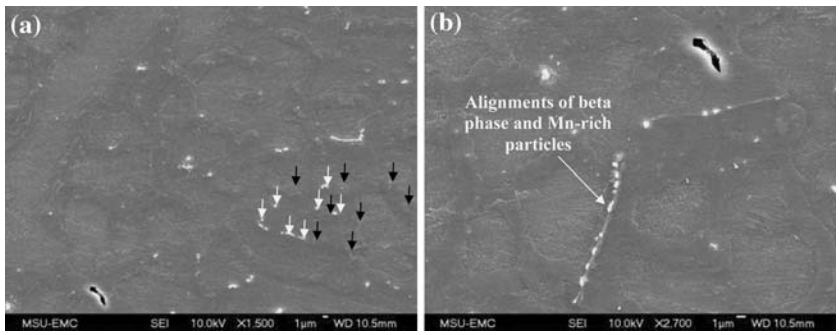

Fig. 3—FEG-SEM micrographs of a polished AM60 sample cut from the grip section of a fractured fatigue specimen showing (*a*) an overall view of the microstructure depicting the Al-rich eutectic layer fully occupying the dendrite cell boundaries, with black and white arrows indicating beta-phase and Mn-rich particles, respectively, and (*b*) a higher-magnification image revealing more abundant formation of the beta phase and Mn-rich phase inside the Al-rich eutectic layer than in the AM50 alloy, with the Mn-rich particles correlating with the beta phase precipitated in the form of strings.

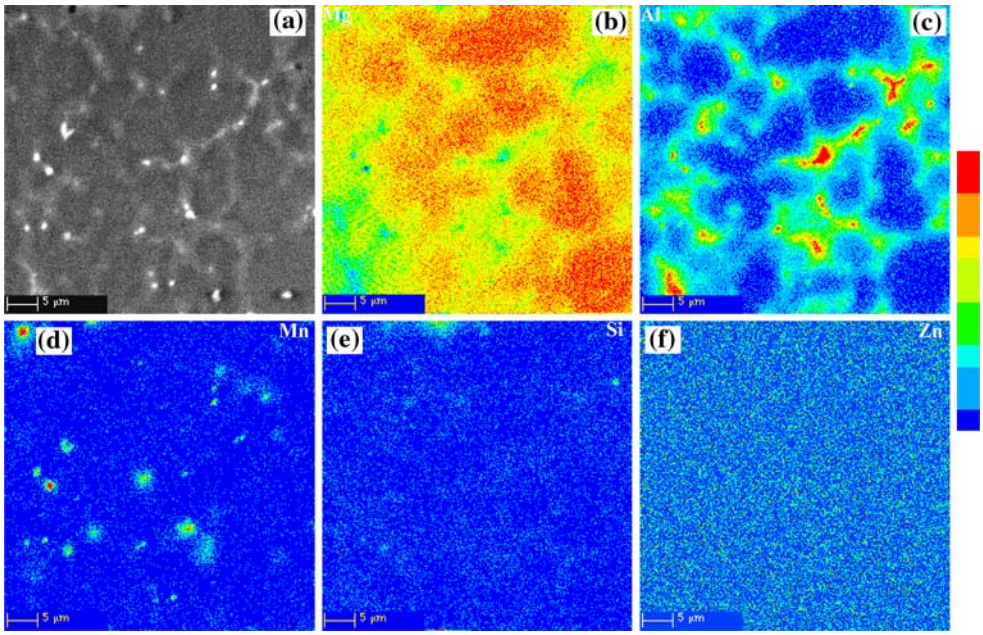

Fig. 4—EPMA X-ray maps of a mirror-finish AM60 sample surface, displayed in (*a*) backscattered mode, revealing (*b*) a Mg-concentration contour, (*c*) an Al-concentration contour delineating the Al-rich eutectic layer, beta phase, and Mn-rich inclusions, with the Al-rich eutectic layer being thicker and more consistent and containing more and larger beta-phase and Mn-rich particles, (*d*) a Mn-concentration contour showing the size and distribution of the Mn-rich inclusions, (*e*) a Si-concentration contour, and (*f*) a Zn-concentration contour.

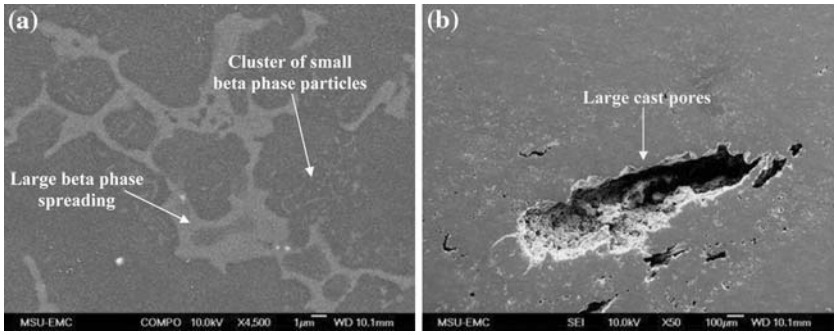

Fig. 5—FEG-SEM micrographs of a polished AZ91 sample cut from the grip section of a fractured fatigue specimen showing (*a*) the Al-rich eutectic layer taking a completely divorced form, with a large and continuous presence of the beta phase and (*b*) large casting pores reaching several millimeters in size.

grains with an average size of 50 μm were also observed.[22] For the AZ91 alloy and the AE44 alloys, the average linear intercept dendrite cell size dropped below 5 μm.

IV. FATIGUE LIFE

The strain amplitudes *vs* cycles to failure are presented for all alloys in Figure 9(a). Figure 9(b) provides the average cycle to failure for each strain amplitude, in an effort to statistically illustrate the difference in fatigue lives among the four alloys. The main point from the fatigue life data is that the AM50 and AM60 alloys showed a better fatigue resistance than did the two other alloys. The lowest fatigue lives were consistently recorded for the AE44 alloy. The AE44 alloy was designed to present the best creep resistance, owing to the lamellar form of the $Al_{11}RE_4$ phase that forms in the interdendritic eutectic.[21] The fatigue life variability increased when the strain amplitude decreased, and this increase in variability intensified for the high-cycle fatigue regime.

In an effort to observe the relevant fatigue crack growth mechanisms associated with each regime, we selected the 0.3-pct strain amplitude condition for our analyses. The representative samples extracted for that purpose are shown in Figure 10 and are designated as sample Z_1 (N_f = 2736) and Z_2 (N_f = 5685) for two AZ91 alloy fatigue lives, E_1 (N_f = 6034) for one AE44 alloy fatigue life, N_1 (N_f = 11649) for one AM60 alloy fatigue life, and M_1 (N_f = 1371) and M_2 (N_f = 4520) for two AM50 alloy fatigue lives.

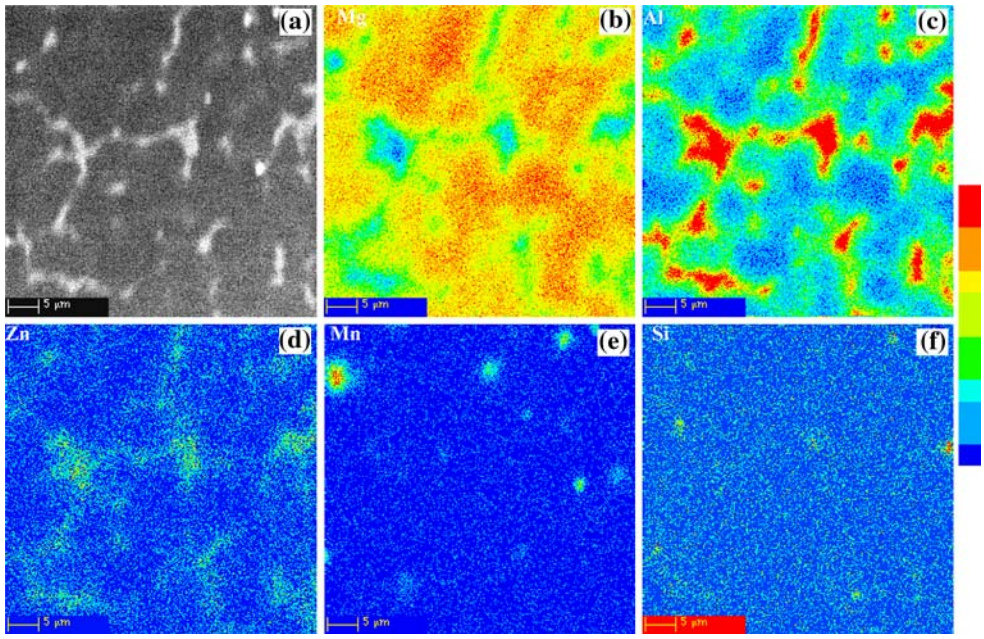

Fig. 6—EPMA X-ray maps of a mirror-finish AZ91 sample surface shown in (*a*) backscattered mode, revealing (*b*) a Mg-concentration contour; (*c*) an Al-concentration contour revealing that the Al-eutectic rich phase takes a completely divorced form in which massive particles of the beta-phase precipitate, (*d*) a Zn-concentration contour revealing that zinc correlates with the beta phase, suggesting that the massive particles could correspond to an $(Al,Zn)_xMg_y$ phase, (*e*) a Mn-concentration contour, and (*f*) a Si-concentration contour.

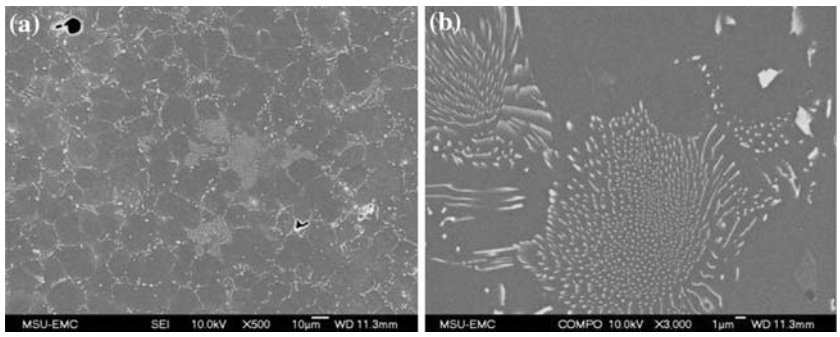

Fig. 7—Backscatter FEG-SEM micrographs of a polished AE44 sample showing (*a*) an overall view of the microstructure depicting shrinkage pores and localization of the $Al_{11}RE_3$ phase within the interdendritic eutectic region and (*b*) a higher-magnification image illustrating the platelet-like shape of the $Al_{11}RE_3$.

V. FRACTOGRAPHY AND DISCUSSION

A detailed fractographic analysis of fatigue crack growth mechanisms in the AM50 alloy was reported in a different article.[17] We briefly restate the relevant results previously stated for this alloy. These results served as a comparison for understanding the mechanisms controlling the fatigue crack growth in the three other Mg alloys.

A. *Fatigue Crack Incubation*

For the AM50 alloy, the fracture surfaces close to the initiation region in samples M_1 and M_2 are presented in the micrographs of Figures 11 and 12, respectively. For both samples, shrinkage pore clusters near the free surface were observed to nucleate the dominant fatigue crack linked to the final failure. These shrinkage pore clusters exhibited the same size and morphology in both samples. However, the overall aspect of the dendrite cells seemed to be smoother in sample M_1 than in sample M_2. This is due to a greater connectivity of the interdendritic shrinkage pores in the shrinkage pore cluster of sample M_1 (Figures 11 and 12). This difference accounts for the greater fatigue life of sample M_2 over sample M_1, since smaller cracks will encounter fewer barriers during their propagation.

For the AM60 alloy, (sample N_1 with $N_f = 11649$), the crack incubated at a shrinkage pore cluster located near the free surface (Figure 13). A similar nucleation phenomenon occurred in sample M_3 ($N_f = 14171$) of the AM50 alloy reported in Reference 17. However, the pore cluster was two orders of magnitude smaller in

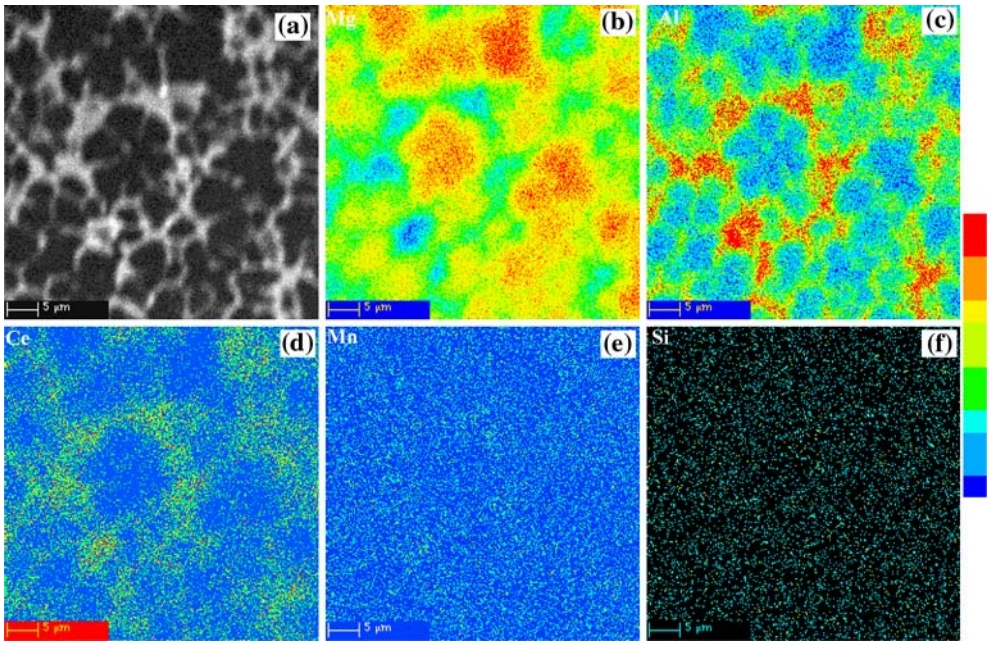

Fig. 8—EPMA X-ray maps of a mirror-finish AE44 sample surface, shown in (*a*) backscattered mode, showing (*b*) an Mg-concentration contour, (*c*) an Al-concentration contour, (*d*) a Ce- concentration contour revealing the nature of the Al/Ce-rich platelets, (*e*) a Mn-concentration contour revealing no presence of the Mn-rich particles consistently found in the AM50, AM60, and AZ91 alloys, and (*f*) a Si-concentration contour showing no presence of this element in the AE44 alloy.

sample M_3[17] than in sample N_1. This difference explains the greater fatigue life for sample M_3. The fatigue crack, however, might have propagated more slowly in sample N_1 than in sample M_3, yet not slowly enough to overshadow the difference caused by the size of the initial fatigue crack.

For the AZ91 alloy, the fracture surface of specimen Z_1 (N_f = 5685) shows that the main fatigue crack nucleated at an agglomeration of large casting pores (Figure 14). These large casting pores were partly contained within the original skin layer of the cast plate and extended into the main bulk microstructure. As typically shown in Figure 5, the AZ91 plates typically exhibited a higher content of large casting pores as compared to the other alloys. The authors recently demonstrated through X-ray computed tomography (XRCT) that AM50 and AM60 exhibited a lower volume of large casting and shrinkage pores than did AZ91 and AE44 cast under the same conditions.[23] This explains the very low fatigue durability of the AZ91 alloy compared to the AM50 and AM60 alloys. The large number of casting pores in specimen Z_1 induced a rough crack propagation path through the coalescence of fatigue cracks that nucleated at neighboring casting and shrinkage pores (Figure 14). Figure 15 shows the fracture surface of specimen Z_2, which had the lowest fatigue life among all the tested AZ91 samples. Here again, the main fatigue crack nucleated at a casting pore that was located within the original skin layer of the cast plate. This pore, however, was significantly more elongated in the crack propagation direction.

For the AE44 alloy, we investigated the E_1 specimen, which had the highest fatigue life among all the tested samples. Figure 16 revealed that the fatigue crack nucleated at a large surface shrinkage pore with a pancake-like shape that extended along the sample free surface. This shrinkage pore is within the original skin microstructure of the cast plate. The length and width of this pore were approximately 1.3 and 0.14 mm, respectively. As can be observed by comparing Figures 1 and 7, the size of the interdendritic shrinkage pores was inversely correlated with the dendrite cell average size. Hence, the beneficial effect of the fine microstructure on fatigue resistance was counterbalanced by the increased propensity to interdendritic shrinkage pore coalescence. The fatigue life of specimen E_1 was below the lowest fatigue life limit of the AM50 and AM60 alloy specimens.

B. *Fatigue Crack Propagation*

1. *The AM50 alloy*

In Reference 17, we observed that, at very low crack tip driving forces, the MSC showed preferential propagation at the Al-rich eutectic phase/α-Mg dendrite cell interface (Figure 17(a)). The MSC were susceptible to following important meandering paths, depending on the size and morphology of the dendrite cell ahead of the crack tip. At an intermediate stage of fatigue life corresponding to approximately to 100 to 150 μm of crack propagation, the driving force of the PSC seemed to be sufficient to deflect the crack into the Al-rich eutectic. In this eutectic, the PSC advanced by a debonding mechanism between fine persistent slip bands formed by a dislocation pile-up phenomenon (Figure 17(b)).[20] The effect of the β-phase particles at

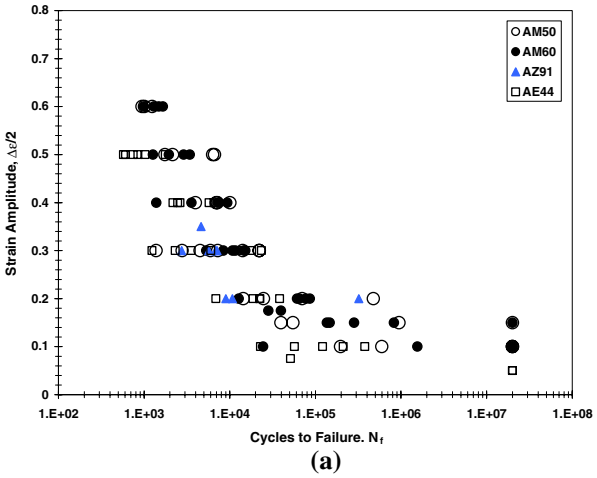

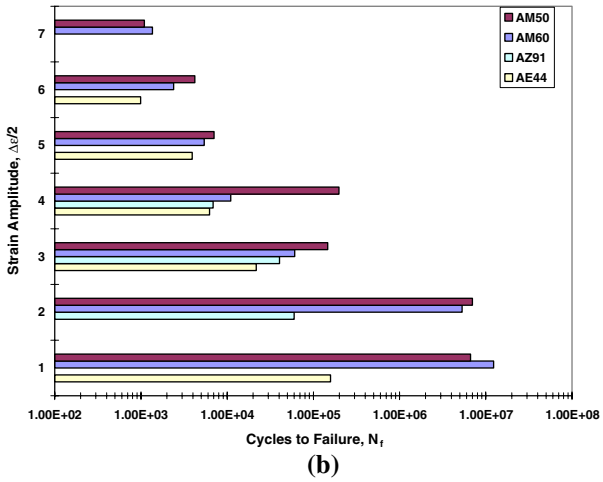

Fig. 9—Fatigue test results of AM50, AM60, AZ91, and AE44 magnesium alloys tested using rectangular specimens at a frequency of 0.5 Hz with an R ratio of −1 showing (*a*) strain-life data for each specimen and (*b*) data on average cycles to failure illustrating that AM50 consistently exhibited a better fatigue resistance followed immediately by AM60, and that the AE44 showed the lowest fatigue life followed immediately by AZ91.

this important stage of the fatigue crack propagation can be both beneficial and detrimental. The β phase could be detrimental because this phase is brittle and susceptible to fracture ahead of the crack tip and, as such, provides weak resistance and easy possible paths for crack propagation. A potential beneficial effect is that the fractured particles attract and force the PSC to remain in the eutectic layer, which appears to be more resistant to fatigue crack propagation.[17] The PSC would encounter more intact particles within the eutectic. As a result, the PSC would be forced to meander around these particles, thus reducing the crack tip opening displacement. In the long crack fatigue regime, the effect of the associated widespread plasticity induced a mixed interdendritic-transdendritic crack propagation mode. The interdendritic propagation was predominantly due to the fragility of the β phase. The transdendritic propagation involved several tens of dendrite cells, which resulted in a sawtooth pattern

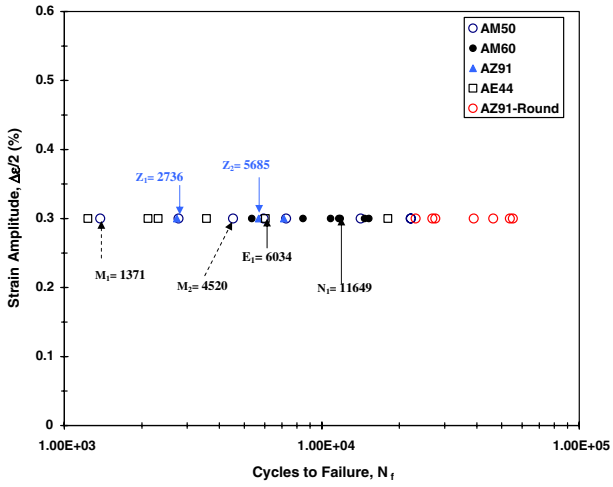

Fig. 10—Strain-life data of AM50, AM60, AZ91, and AE44 magnesium alloys tested using rectangular samples at a 0.3-pct strain amplitude and a frequency of 0.5 Hz with an R ratio of −1; the arrows indicate the samples subjected to fractography analyses.

(Figure 17(c)). The tendency for the transdendritic propagation was greater near shrinkage pores.

2. *The AM60 alloy*

For the AM60 alloy, the small crack propagation occurred in a way that was similar to that observed for the AM50 alloy. At the edge of the shrinkage pore cluster, where the fatigue crack incubated, smooth dendrite cells were observed to be covered with very fine striations, as illustrated in Figure 18. The forefront of the main fatigue crack was very rough, illustrating a meandering through the dendrite cell, following the Al-eutectic rich layer/dendrite cell interface. Some dendrite cells seemed, however, to be more flat, due to very fine persistent slip bands emerging at the free surface. This phenomenon is a characteristic of the intermediate stage of propagation observed for the AM50 alloy. In this stage, the corresponding PSC cut through the Al-rich eutectic layer. For the AM60 alloy, the early stage of the crack propagation seemed to be characterized by a lesser tendency toward the interfacial small crack advance, as compared to that of the AM50 alloy. This is probably due to a more pronounced presence of the brittle phase that fractured at smaller driving forces and that, as a result, inclined the crack to deflect rapidly into the eutectic layer. Within this eutectic, the higher concentration of the β-phase particles compared to the AM50 alloy implies that more particles would fracture in the AM60 alloy. As a result, for the AM60 alloy, the effect of the β phase is more detrimental than it is beneficial, as compared to the effect for the AM50 alloy.

After approximately 100 μm of propagation (*vs* 200 to 300 μm for sample M_3[17]) away from casting and shrinkage pores, the fatigue crack exhibited a relatively flat and smooth surface covered by coarse persistent slip bands, twins, and cleavage-like bands, as shown in Figure 19. These crack propagation mechanisms corresponded to the long fatigue crack growth regime. In the AM50 alloy, this stage was characterized by a mixed

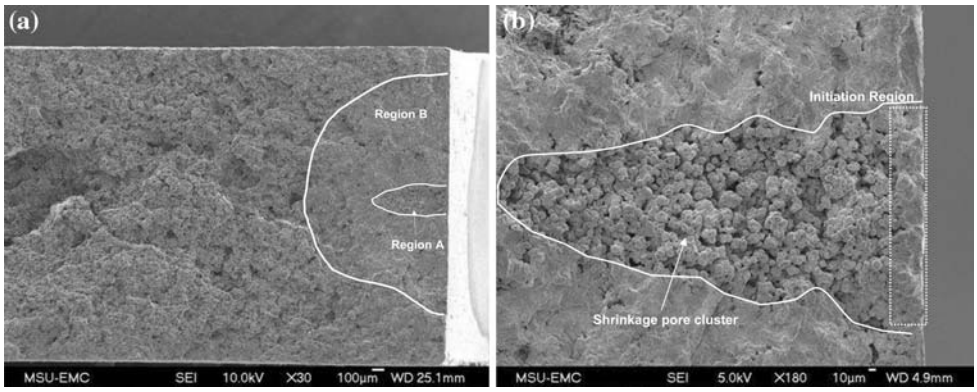

Fig. 11—FEG-SEM fracture surfaces of sample M_1 (N_f = 4520) showing (*a*) an overall view of the fracture surface delineating the fatigue crack propagation and (*b*) a higher magnification of Region A, which corresponds to the crack propagation in a shrinkage pore cluster.

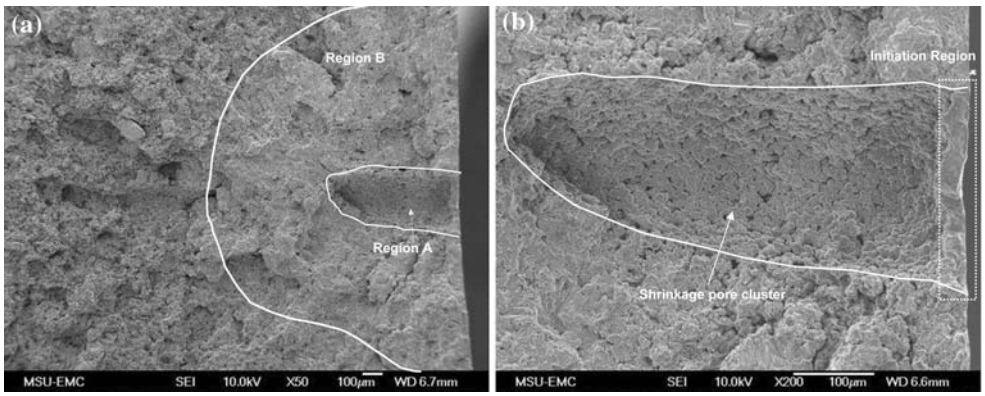

Fig. 12—FEG-SEM fracture surfaces of sample M_2 (N_f = 1379) showing (*a*) an overall view of the fracture surface delineating the fatigue crack propagation and (*b*) a higher magnification of Region A, which corresponds to the crack propagation in a shrinkage pore cluster.

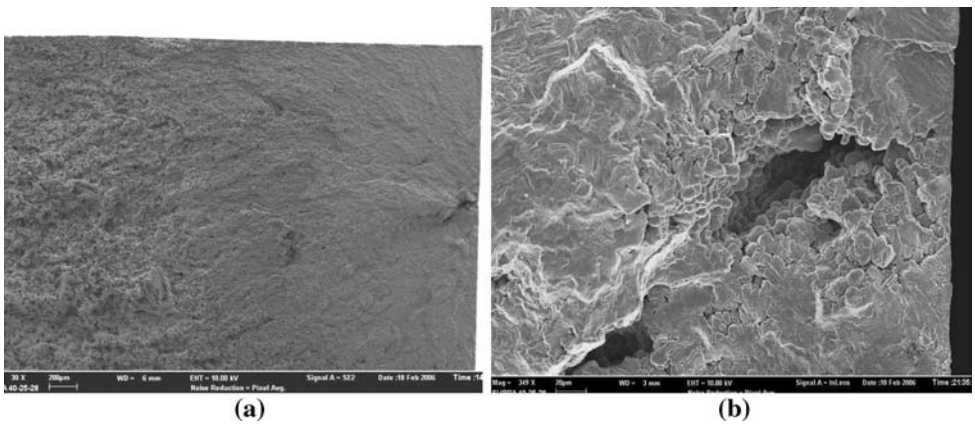

Fig. 13—FEG-SEM fracture surfaces of sample N_1 (N_f = 11649) cut from an AM60 alloy plate showing (*a*) an overall view of the fracture surface and (*b*) a higher-magnification view of the region, including the surface shrinkage pore that nucleated the main fatigue crack.

crack propagation mode with a preponderance of the interdendritic mode. This interdendritic long crack propagation mode left the surface mostly covered by fractured particles in the Al-rich eutectic. In the AM60 alloy, however, despite the higher content of the brittle β-phase particles, the LC showed significantly less tendency for interdendritic propagation, and the fracture surface remained more flat and homogeneous.

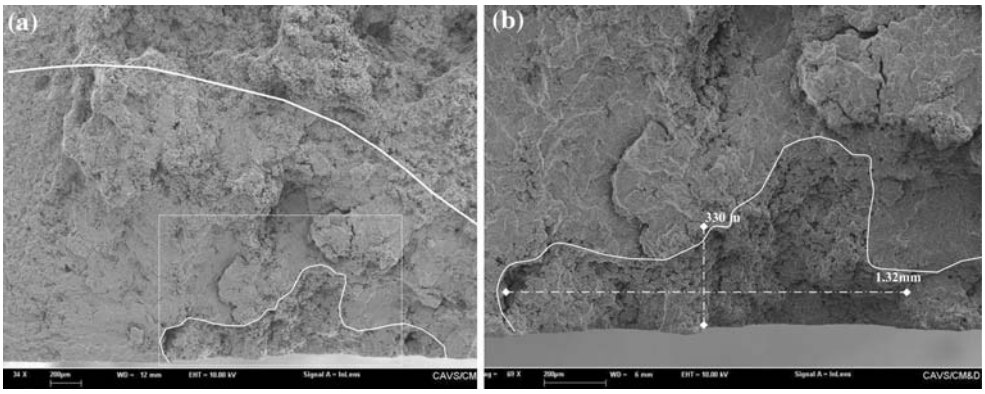

Fig. 14—FEG-SEM fracture surfaces of sample Z_2 (N_f = 5685) cut from an AZ91 alloy plate showing (*a*) an overall view of the fracture surface and (*b*) a higher magnification of the region, including the casting pore that nucleated the main fatigue crack. Note that the casting pore extends along the sample free surface.

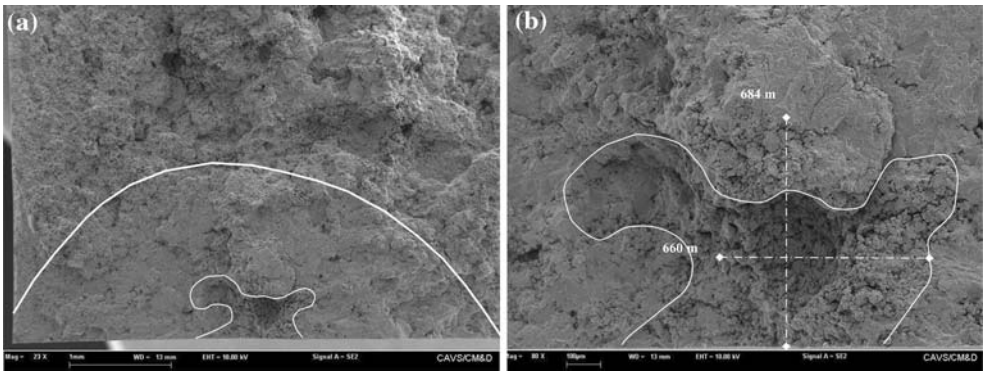

Fig. 15—FEG-SEM fracture surfaces of sample Z_2 (N_f = 2736) cut from an AZ91 alloy plate showing (*a*) an overall view of the fracture surface and (*b*) a higher magnification of the region, including the casting pore that incubated the main fatigue crack. Note that the casting pore extends perpendicular to the sample free surface.

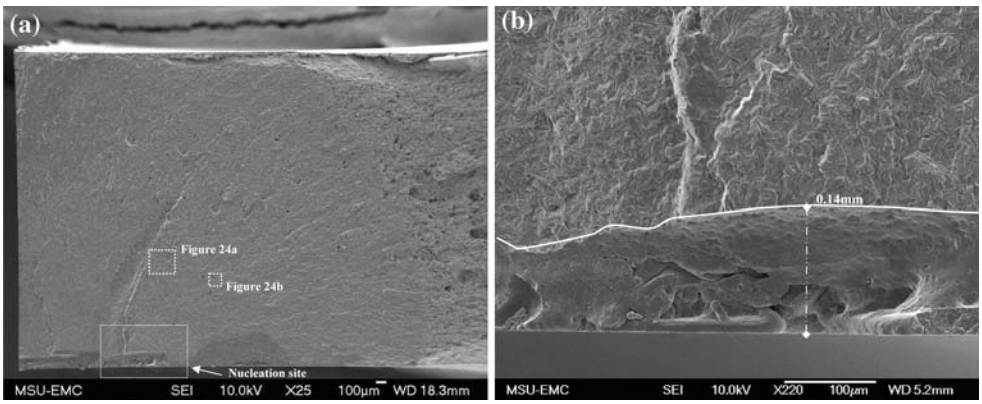

Fig. 16—FEG-SEM fracture surfaces of sample E_1 (N_f = 6085) cut from an AZ91 alloy plate showing (*a*) an overall view of the fracture surface and (*b*) a higher magnification of the region, including the large surface shrinkage pore that nucleated the main fatigue crack. Note that the pore extends along the sample free surface.

3. *The AZ91 alloy*

Figures 14 and 15 revealed that the large incubated cracks in the AZ91 alloy induced a noticeable acceleration of the onset of the long fatigue crack propagation regime. Also, the presence of coarse interdendritic β-phase nodules at the expense of the Al-rich eutectic layer seemed

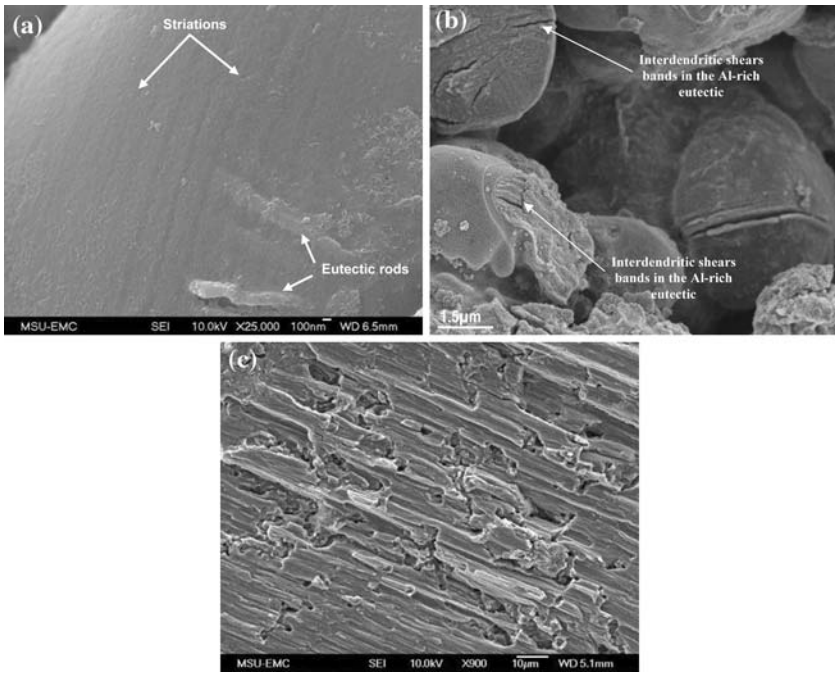

Fig. 17—FEG-SEM fracture surfaces of sample M_4 (N_f = 7269) reported in Reference 17 and sample M_1 (N_f = 4520) showing (*a*) a dendrite cell close to the initiation site covered with fine striations revealing microstructurally small crack propagation between two cohesive dendrites along the Al-rich eutectic layer/dendrite cell interface, (*b*) physically small crack propagation through the Al-rich eutectic layers leaving the entire dendrite volume, but with a flat surface, and (*c*) a high-magnification view of a shear band pattern crossing several tens of dendrite cells, as evidenced by the high density of individual interdendritic shrinkage pores.

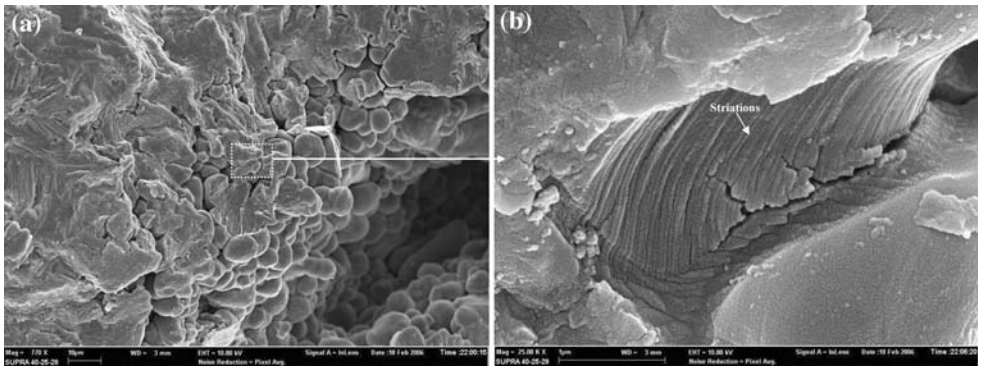

Fig. 18—FEG-SEM fatigue fracture surfaces of sample N_1 (N_f = 11649) cut from an AM60 alloy plate and showing (*a*) an overall view of the region surrounding the shrinkage pore cluster nucleating the main fatigue crack and (*b*) a higher magnification of the region delineated in (a) depicting round and smooth dendrite cells covered with fine striations characteristic of the microstructurally small crack propagation at the Al-rich eutectic layer/dendrite cell interface.

to increase stress concentrations at the dendrite cell boundaries. This is evinced by the localization of persistent slip bands at the vicinity of β-phase strings (Figure 20). Moreover, an important number of large casting and shrinkage pores existed at the fracture surface (Figures 14 and 15).

The long fatigue crack propagation regime in the AZ91 alloy was mainly characterized by a mixed transdendritic-interdendritic mode. Figure 21 shows that the interdendritic propagation was substantiated by the presence of smooth β-phase particles at the fracture surface. For the same specimen, Figure 22(a) shows many ''deep'' cracks in the direction of the main fatigue crack propagation. These deep cracks are in-plane cracks that emerged at the fracture surface, which is an atypical phenomenon. They were bordered with fine striation-containing nodules revealing the creation of subsidiary small cracks that propagated over a shorter range (Figure 22(b)). The deep cracks were, in all likelihood, the result of damage induced by

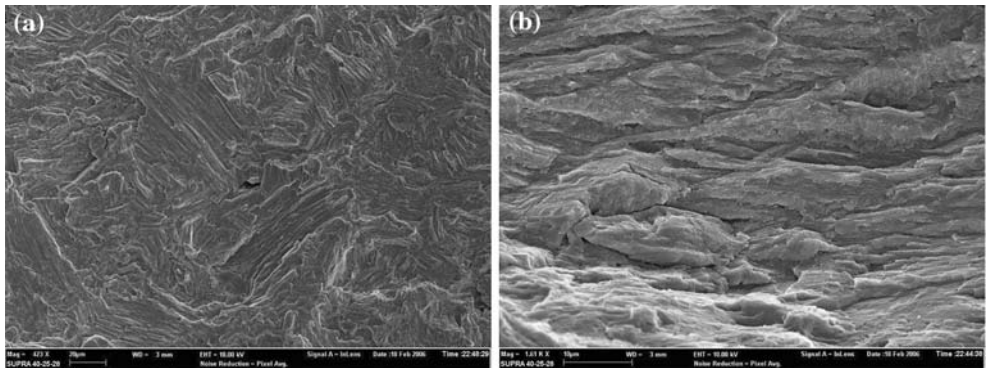

Fig. 19—FEG-SEM fracture surfaces of sample N_1 (N_f = 11649) showing (*a*) transdendritic shear nodules in the long crack fatigue regime spreading over several tens of dendrites and (*b*) a cleavage-type fracture in the long crack fatigue regime spreading over several dendrite cells.

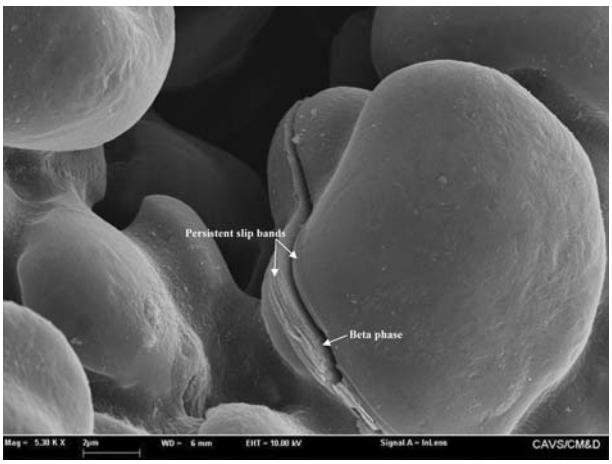

Fig. 20—A FEG-SEM fracture surface of sample Z_2 (N_f = 5685) cut from an AZ91 alloy plate showing the localization of persistent slip bands at the vicinity of an interdendritic beta-phase string.

coalescence mechanisms between relatively large secondary cracks evolved from casting and shrinkage pores. In marked contrast to the AM50 and AM60 alloys, we did not observe in the AZ91 alloy large transdendritic persistent slip band nodules around casting and shrinkage pores extending over several tens of dendrite cells. Rather, interdendritic propagation exposing smooth β-phase strings accompanied by the presence of fine slip bands and striations occurred in the surrounding areas of bulk shrinkage and casting pores (Figure 21). This interdendritic propagation revealed that the enhanced porosity and β-phase precipitates in the AZ91 alloy promoted damage mechanisms that are characteristic of the low-cycle fatigue regime. The absence of the large shearing nodules in the AZ91 alloy may be due to more than the pronounced presence of casting pores.

We actually performed fatigue tests on an AZ91 alloy that was directly cast into the form of round fatigue test specimens and that exhibited lesser porosity as compared to that observed in the AZ91 based plates. The fractography analyses on these specimens showed no presence of extra large shearing nodules analogous to those encountered in the AM50 and AM60 alloys (Figure 23). This finding suggests that the interdendritic β-phase precipitates act as barriers for dislocation pile-up transmission between adjacent dendrite cells.[20] Note that, for these specimens, the main fatigue crack initiated on inclusion clusters formed by surface macrosegregation phenomena, as illustrated in Figure 23.

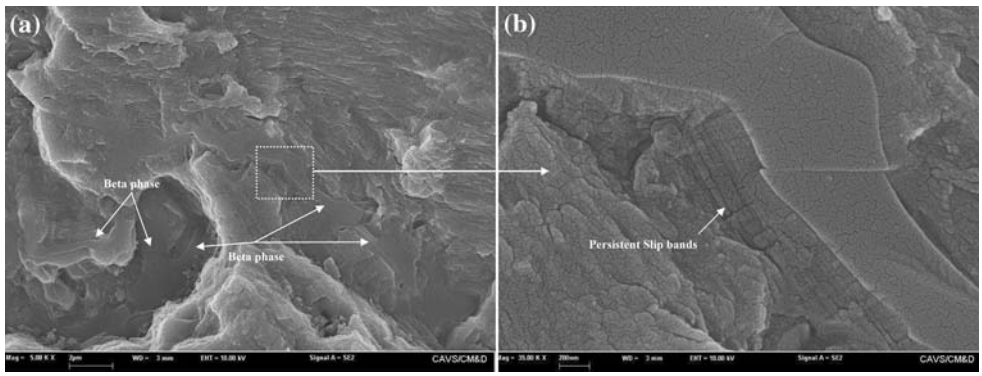

Fig. 21—FEG-SEM fracture surfaces of sample Z_1 (N_f = 2736) cut from an AZ91 alloy plate and showing (*a*) smooth beta-phase precipitates revealing interdendritic and microstructurally small-crack-propagation-related mechanisms at the vicinity of a shrinkage pore cluster encountered 600 μm away from the crack nucleation site and (*b*) a higher magnification of the region highlighted in (a) depicting fine striations around an elongated beta-phase precipitate.

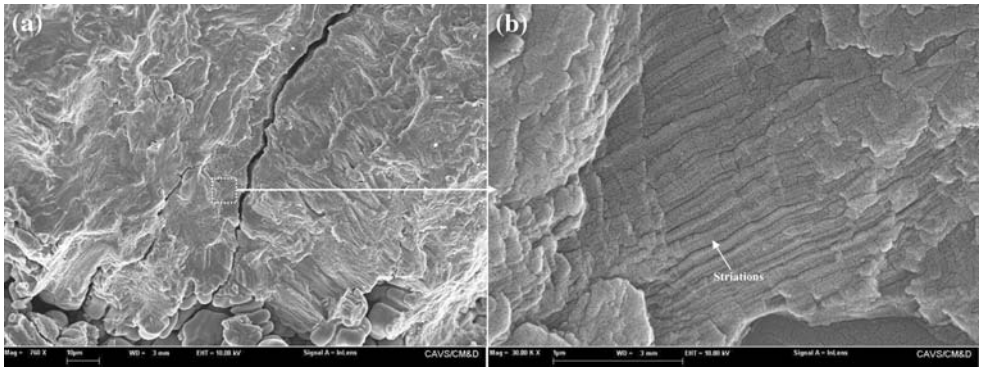

Fig. 22—FEG-SEM fracture surfaces of sample Z_1 (N_f = 2736) cut from an AZ91 alloy plate showing (*a*) an overall view of the region surrounding the casting pore nucleating the main fatigue crack and containing a deep crack and (*b*) a higher magnification of the region delineated in (a) depicting striations of a small crack that most likely incubated from the transversal in-plane deep crack.

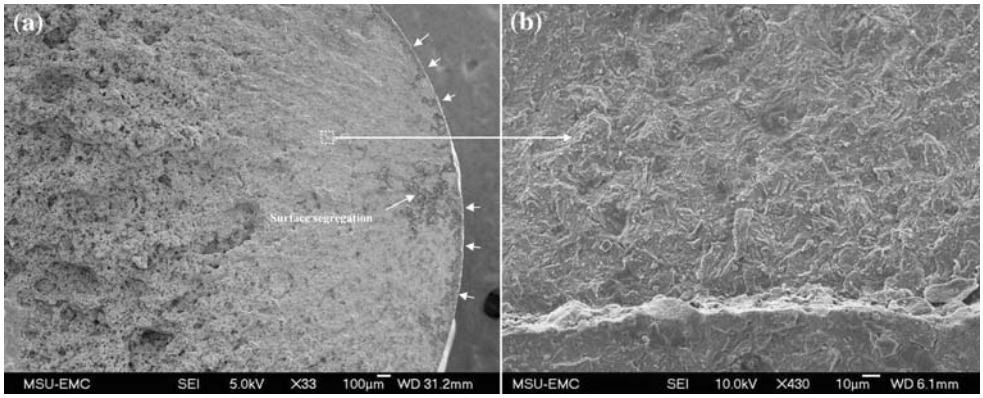

Fig. 23—FEG-SEM fracture surfaces of a round and cast AZ91 sample N_1 showing (*a*) an overall view of the fatigue crack propagation surface illustrating surface segregating particles (arrows) that originated the main crack and (*b*) a higher magnification of the region delineated in (a) representing a typical aspect of the fracture surface associated with the long crack growth regime, in which no extra large persistent slip bands nodules were observed.

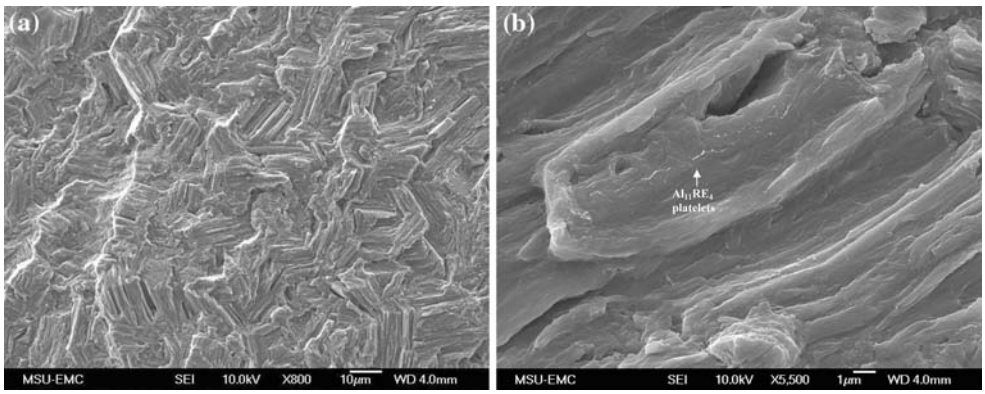

Fig. 24—FEG-SEM fracture surfaces of sample E_1 (N_f = 6034) showing (*a*) a higher magnification of the region delineated in Fig. 16(a) and exhibiting total coverage of the fracture surface by persistent slip/twin band nodules that are the same size as the dendrite cells and (*b*) a higher-magnification view of the region delineated in Fig. 16(a) showing that the thick shear/twin bands were activated in the same direction as that of the $Al_{11}RE_4$ platelet axis.

4. *The AE44 alloy*

Figure 24 reveals that the fatigue crack nucleated at the vicinity of a surface shrinkage pore. Afterward, the fatigue crack totally propagated in a transdendritic mode over the entire fracture surface. The persistent slip/twin bands exhibited a thickness that spanned a

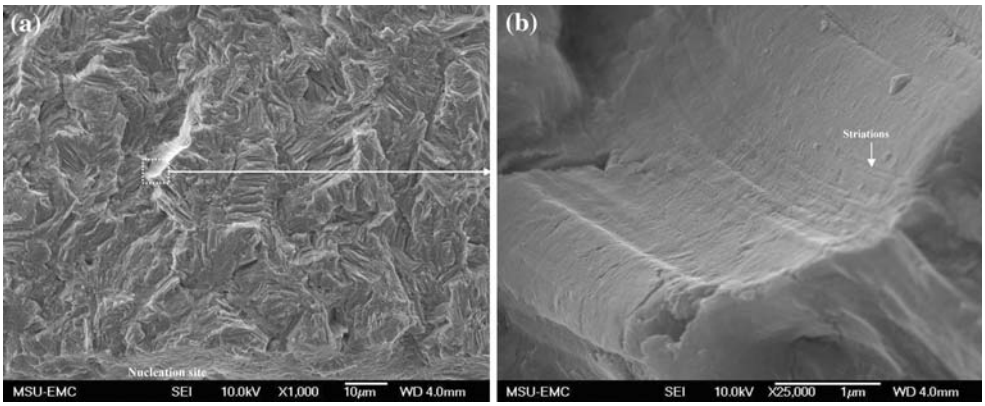

Fig. 25—FEG-SEM fracture surfaces of sample E_1 (N_f = 6034) showing (*a*) an overall view close to the nucleation region and (*b*) a higher magnification of the region delineated in (a) displaying fine striations corresponding to the initial stages of fatigue crack propagation.

range from 100 nm to a few micrometers. The main fatigue crack cut straight through the persistent slip/twin bands and left visible striations at the beginning of propagation (Figure 25), but no striations were detected after approximately 200 μm of crack extension. This is probably due to the fatigue crack propagation rate becoming greater than the size of a typical persistent slip/twin band. As with the AZ91 alloy, the persistent slip/twin bands were confined within areas in the range of the dendrite cell size, and no extra large shearing band nodules similar to those observed in the AM50 and AM60 alloys were observed. For the AZ91 alloy, we have suggested that the lamellar β phase localized at the dendrite cell boundaries acts as a barrier to dislocation migration across the dendrite cells. Similar mechanisms seemed to have operated in the AE44 alloy, in view of the interdendritic eutectic lamellar phase $Al_{11}RE_4$. This phase may have played a major role in blocking dislocation movement. One important result of our observations is that the fatigue crack advanced in a very soft material with higher rates than those observed for the AM50, AM60, and AZ91 alloys. Indeed, the relatively low percentage of Al in this alloy, combined with the higher tendency of rare earth elements to attract Al only in the interdendritic regions, resulted in poorer Al solid solution Mg dendrite cells than those in the three other studied alloys (Figure 26).

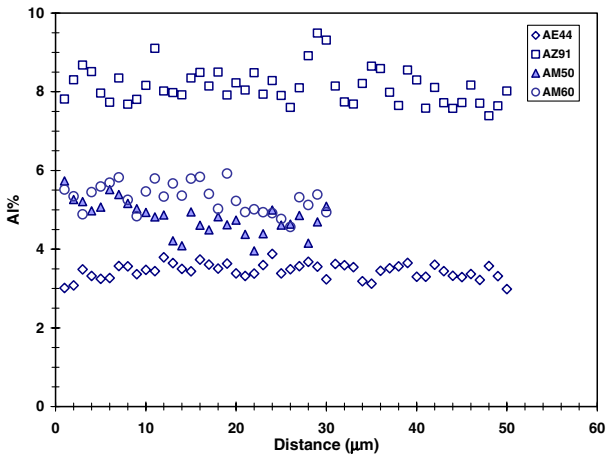

Fig. 26—Quantitative Al concentration profile for all investigated alloys obtained using EPMA. The distance between two adjacent analyzed points was 1 μm.

VI. SUMMARY

The effects of microstructure on fatigue crack growth mechanisms were studied for AM50, AM60, AZ91, and AE44 Mg alloys. The proposed fatigue mechanisms are summarized in Table II. We distinguish two main conclusions: four main stages observed for each alloy and the structure-property relations for fatigue crack incubation and small crack growth.

A. *Multistage Fatigue Regimes*

The observed fatigue crack propagation mechanisms in the AM50 and AM60 Mg alloys showed four fatigue life stages:

1. an incubation stage;
2. a microstructurally small crack stage, in which the crack advanced at the Al-rich eutectic/dendrite cell interface;
3. a physically small crack stage, in which the crack advances within the eutectic; and
4. a long crack regime, in which the crack propagation was transdendritic or interdendritic.

In the AZ91 Mg alloy, the coalescence of several cracks was observed because of the high porosity levels. This coalescence was promoted by the fracture of the β-phase. The β-phase was present in the form of small particles within the cell matrix, but formed continuous strings at the cell boundaries. We observed, however, that the small cracks propagated around the β-phase particles, and this regime may predominate when less severe porosity is present. In the AE44 Mg alloy, the propagation was completely transdendritic. This transdendritic propagation arose because a relatively soft matrix and a very thin $Al_{11}RE_4$ lamellar phase offered little resistance to even small crack growth.

Table II. Qualitative Summary of Microstructural Effects on Fatigue Crack Growth over the Four Distinct Regimes

	AM50				AM60				AZ91				AE44			
Attributes	INC	MSC	PSC	LC	INC	MSC	PSC	LC	INC	MSC	PSC	LC	INC	MSC	PSC	LC
HSP	− −	− −	−	−	− −	− −	−	−	− − −	− − −	− −	−	− − −	− −	−	− −
CP	−	−	− −	− −	−	−	− −	− −	− − −	−	− −	− −	−	−	− −	− −
Al-RSSL	n/a	+ + +	+ +	+	n/a	+ +	+	+ +	n/a	n/a	n/a	n/a	n/a	n/a	n/a	n/a
BP	n/a	+	+	−	n/a	+	+−	−	n/a	−+	−	− −+	n/a	n/a	n/a	n/a
Mn-RI	− − −	−	−	−	− − −	−	−	−	− −	−	−	−	n/a	n/a	n/a	n/a
$Al_{11}RE_4$	n/a	n/a	n/a	n/a	n/a	n/a	n/a	n/a	n/a	n/a	n/a	n/a	n/a	+	−	− −+
DCS	+	−	−	+	+	−	−	+	−	−	−	−	n/a	+	−	−
SS	n/a	n/a	n/a	n/a	n/a	n/a	n/a	n/a	− − −	− −	−	n/a	n/a	n/a	n/a	n/a

B. *Effect of Structure-Property Relationships on Fatigue Crack Growth*

The lowest fatigue resistance was recorded for the AE44 alloy; the next lowest was recorded for the AZ91 alloy. The AM50 alloy showed the best fatigue durability, followed by the AM60 alloy.

We first compared the fatigue lives of the AE44 and AZ91 alloys, because these two alloys showed large pore size and content and smaller dendrite cell size, as compared to the AM50 and AM60 alloys. Although the AE44 alloy had a smaller pore size and content, it showed a lower fatigue resistance than did the AZ91 alloy, probably because of the lower content of Al in the AE44 matrix, augmented by the effect of rare earth elements, which combined with Al in the eutectic regions. These two mechanisms contributed to the reduction of the solid solution strengthening effect of Al.

The pore size and content in the AE44 and AZ91 alloys were greater than those in the AM50 and AM60 alloys. The effect of porosity on fatigue life was preponderant, because it counterbalanced the beneficial high Al content, especially in the AZ91 alloy. The effect of large pores is primarily on the incubation life, because of their higher stress concentration. The other noticeable effect of large pore size is the substantial reduction of the MSC regime life, because a larger pore size will induce an initial crack of greater length. Similarly, higher pore content is detrimental to fatigue resistance, because it promotes easier paths for crack propagation in the LC regime.

However, the high Al content in the AZ91 alloy was revealed to promote precipitation of continuous strings of the brittle β phase and to eliminate the Al-rich eutectic layer. The Al-rich eutectic layer was observed to be beneficial during the small crack regime, for the AM50 and AM60 alloys.

The lower Al content in the AM60 alloy compared to that in the AZ91 alloy gave rise to an Al-rich solid solution layer in the dendrite cell boundaries with less uniformly dispersed precipitation of the β phase. The less uniformly dispersed precipitation of the β phase reduced the pinning effect of the dendrite cell boundaries that operated during the primary recrystallization following the casting process. As a result, the grains observed in the AM60 alloy were coarser than those in the AZ91 alloy. The coarser grains reduced the propensity of the interdendritic shrinkage pores to coalesce. These effects contributed to the increased fatigue resistance of the AM60 alloy as compared to AZ91 and AE44 alloys. The effect of the β-phase particles at the PSC stage of the fatigue crack propagation can be both beneficial and detrimental. The detrimental effect was correlated with the brittle nature of this phase, which fractured ahead of the crack tip and provided weak paths for the crack advance. The beneficial effect occurred because the fractured particles attracted and forced the fatigue crack to remain in the eutectic layer and meander around the particles.

The beneficial effects of the β-phase particles were maximized for the AM50 alloy in that the Al-rich solid solution in Mg was thicker and contained fewer particles. These characteristics offered a relatively better fatigue performance for the AM50 alloy than for the AM60, AZ91, and AE44 alloys.

ACKNOWLEDGMENTS

The authors thank the Center for Advanced Vehicular Systems (CAVS), Mississippi State University (MSU), United States Automotive Materials Partenership (USAMP), and the Structural Casting Magnesium Development (SCMD) group for the work performed in this study. The authors are also grateful for the fruitful conversations and advice of Dr. John Berry, MSU.

NOMENCLATURE

DESIGNATIONS

HSP	hydrogen shrinkage pores
CP	casting pores
Al-RSSL	Al-rich solid solution layer
BP	beta phase
Mn-RI	Mn-rich inclusions
DCS	dendrite cell size
SS	surface segregations

$Al_{11}RE_4$	stoichiometry associated in the literature with the observed lamellar-like intermetallic in the AE44 alloy
INC	incubation regime
MSC	microstructurally small crack regime
PSC	physically small crack regime
LC	long crack regime
+	beneficial for fatigue resistance
–	detrimental for fatigue resistance
n/a	not applicable

COMMENTS: AM50 ALLOY

HSP	more detrimental effects on incubation and MSC; several cracks can nucleate and rapidly coalesce to shorten or bypass the MSC
CP	more detrimental effects for PSC and LC; maybe shielding effect (+)
Al-RSSL	**Thick layer in the range of 3μm:**
MSC	interfacial propagation and shielding effect
PSC	interdendritic propagation; Al-RSSL is stronger
LC	blocks, but slightly, the dislocation pile-up transmission; dragging effect
BP:	
MSC	interfacial propagation, strengthening the Al-RSSL and shielding effect
PSC	interdendritic propagation, beta-phase fracture and forces crack to remain in the Al-RSSL
LC	fractures and provides weak paths for crack propagation
Mn-RI, for all alloys except AE44:	
INC	large particles accelerating nucleation life
MSC	weak interface that easily debonds
PSC	particles easily fracture
LC	particles easily fracture
DSC, AM50 and AM60 (large dendrite cells):	
INC	large DC then fewer Mn-rich inclusions
MSC	large DC, then do not force the crack to meander significantly
PSC	large DC, then do not force the crack to meander significantly
LC	large DC, then less fractured beta-phase particles

COMMENTS: AM60 ALLOY (ONLY DIFFERENCES COMPARED TO THE AM50 ALLOY)

Al-RSSL	**Thick layer in the range of 3 μm:**
MSC	interfacial propagation, but beta phase starts to fracture
PSC	interdendritic propagation; Al-RSSL is stronger
LC	blocks better dislocation pile-up transmission, because more BP (fewer large PSCB nodules)
BP:	
MSC	interfacial propagation, strengthening the Al-RSSL
PSC	interdendritic propagation, beta-phase fractures and forces crack to remain in the Al-RSSL, but more fracture, then shorter PSC than in AM50
LC	fractures and provides weak paths for crack propagation

COMMENTS: AZ91 ALLOY (ONLY DIFFERENCES COMPARED TO THE AM50 ALLOY)

HSP	**more shrinkage pores**
CP	**more casting pores**
BP (continuous interdendritic layer and transdendritic particles of beta phase):	
MSC	transdendritic propagation; beta phase in particulate form forces the crack to meander, but in the interdendritic regions, beta phase is source of stress concentration
PSC	beta phase easily fractures and provides weak paths for crack propagation
LC	beta phase easily fractures and provides weak paths for crack propagation, but no large transdendritic persistent slip bands are observed, so action on dislocation pile-ups at dendrite cell boundaries
DSC (fine microstructure):	
MSC	small dendrite cells, then shorter MSC, because many crack nucleate from fractured beta phase and then coalesce
PSC	small dendrite cells, then more fractured beta phase and more stress concentrations
LC	small dendrite cells, then more fractured beta phase and more stress concentrations
SS:	
INC	SS particles accelerate incubation life
MSC	provide weak interfaces
PSC	provide weak interfaces

AE44 ALLOY (ONLY DIFFERENCES COMPARED TO THE AM50 ALLOY)

HSP	**more shrinkage pores**
$Al_{11}RE_4$:	

MSC	forces the crack to meanders
PSC	promotes plasticity and persistent slip bands formation along $Al_{11}RE_4$ platelets
LC	promotes plasticity and persistent slip bands formation along $Al_{11}RE_4$ platelets, but no large transdendritic persistent slip bands are observed, so action on dislocation pile-ups at dendrite cell boundaries
DSC (fine microstructure):	
MSC	small dendrite cells, then more meandering and deceleration because of the $Al_{11}RE_4$ platelets
PSC	small dendrite cells, then more fractured beta phase and more stress concentrations
LC	small dendrite cells then more fractured beta phase and more stress concentrations

REFERENCES

1. D.J. Sakkinen: SAE Technical Paper 940779, SAE, Detroit, MI, 1994, pp. 71–82.
2. D.J. Stratford: *Magnesium and Its Alloys*, Institution of Metallurgists, Loughborough University, England, Course Volume: Series 3 (20), 1983, pp. 132–37.
3. D.L. Goodenberger and R.I. Stephens: *SAE Trans.: J. Eng. Mater. Technol.*, 1993, vol. 115 (4), pp. 391–97.
4. G. Song and StJohn: *J. Light Met.*, 2002, vol. 2, pp. 1–16.
5. V.A. Marichev and S.A. Shipilov: *Sov. Mater. Sci.*, 1986, vol. 22 (3), pp. 240–44.
6. G.L. Makar, J. Kruger, and K. Sieradzki: *Corros. Sci.*, 1993, vol. 34 (8), pp. 1311–42.
7. H. Mayer, M. Papakyriacou, B. Zettl, and S.E. Stanzl-Tschegg: *Int. J. Fatigue*, 2003, vol. 25 (3), pp. 245–56.
8. M.F. Horstemeyer, N. Yang, K. Gall, D.L. McDowell, J. Fan, and P.M. Gullett: *Acta Mater.*, 2004, vol. 52 (5), pp. 1327–36.
9. K. Gall, G. Biallas, H.J. Maier, M.F. Horstemeyer, and D.L. McDowell: *Mater. Sci. Eng., A*, 2005, vol. 396, pp. 143–54.
10. M.F. Horstemeyer, N. Yang, K. Gall, D. McDowell, J. Fan, and P. Gullett: *Fatigue Fract. Eng. Mater. Struct.*, 2002, vol. 25 (11), pp. 1045–56.
11. T.-S. Shih, W.-S. Liu, and Y.-J. Chen: *Mater. Sci. Eng., A*, 2002, vol. 325, pp. 152–62.
12. L. Zheng, W. Zhongguang, W. Yue, and L. Zhongyang: *J. Mater. Sci. Lett.*, 1999, vol. 18 (19), pp. 1567–69.
13. W.T. Donlon, C. Paige, C.J. Morris, and J.E. Allison: *Aluminum and Magnesium for Automotive Applications*, Minerals, Metals and Materials Society, AIME (USA), Cleveland, OH, 1996, pp. 17–27.
14. T.M. Yue, H.U. Ha, and N.J. Musson: *J. Mater. Sci.*, 1995, vol. 30 (9), pp. 2277–83.
15. A.K. Dahle, Y.C. Lee, M.D. Nave, P.L. Schaffer, and D.H. StJohn: *J. Light Met.*, 2001, vol. 1 (1), pp. 61–72.
16. X.-S. Wang, X. Lu, and D.-H. Wang: *Mater. Sci. Eng., A*, 2004, vol. 364, pp. 11–16.
17. H. El Kadiri, Y. Xue, M.F. Horstemeyer, J.B. Jordon, and P.T. Wang: *Acta Mater.*, 2006, vol. 54, pp. 5061–76.
18. D.L. McDowell, K. Gall, M.F. Horstemeyer, and J. Fan: *Eng. Fract. Mech.*, 2003, vol. 70 (1), pp. 49–80.
19. G.R. Patel and A.M. Gokhale: *Scripta Mater.*, 2005, vol. 52 (10), pp. 1063–68.
20. R.M. Wang, A. Eliezer, and E.M. Gutman: *Mater. Sci. Eng., A*, 2003, vol. 355, pp. 201–07.
21. *ASM Handbook*, vol. 9, *Metallography and Microstructures*, 2004, ASM, Materials Park, OH, p. 813, Fig. 27.
22. H.I. Laukli, O. Lohne, and L. Arnberg: *Shape Casting: The John Campbell Symp*, TMS, Warrendale, PA, 2005, pp. 263–72.
23. M.F. Horstemeyer, D. Oglesby, J. Fan, H. El Kadiri, Y. Xue, C. Burton, P.M. Gullett, B. Jelinek, M.K. Jones, A.L. Oppedal, S.G. Kim, E.B. Marin, D.L. McDowell, K. Gall, and N. Yang: *CAVS/MSU Report Prepared for USCAR/USAMP-AMD*, Center for Advanced Vehicular Systems (CAVS), Starkville, MS, 2006.